

Ion pair sites for efficient electrochemical extraction of uranium in real nuclear wastewater

Received: 11 December 2023

Accepted: 6 May 2024

Published online: 16 May 2024

 Check for updatesTao Lin¹, Tao Chen¹, Chi Jiao², Haoyu Zhang¹, Kai Hou¹, Hongxiang Jin¹, Yan Liu²✉, Wenkun Zhu¹✉ & Rong He¹✉

Electrochemical uranium extraction from nuclear wastewater represents an emerging strategy for recycling uranium resources. However, in nuclear fuel production which generates the majority of uranium-containing nuclear wastewater, fluoride ion (F⁻) co-exists with uranyl (UO₂²⁺), resulting in the complex species of UO₂F_x and thus decreasing extraction efficiency. Herein, we construct Ti^{δ+}-PO₄³⁻ ion pair extraction sites in Ti(OH)PO₄ for efficient electrochemical uranium extraction in wastewater from nuclear fuel production. These sites selectively bind with UO₂F_x through the combined Ti-F and multiple O-U-O bonds. In the uranium extraction, the uranium species undergo a crystalline transition from U₃O₇ to K₃UO₂F₅. In real nuclear wastewater, the uranium is electrochemically extracted with a high efficiency of 99.6% and finally purified as uranium oxide powder, corresponding to an extraction capacity of 6829 mg g⁻¹ without saturation. This work paves an efficient way for electrochemical uranium recycling in real wastewater of nuclear production.

Uranium is the key fundamental resource in the nuclear industry¹⁻³. With the development of the nuclear industry, uranium resources in terrestrial ore will be depleted within less than a century, accompanied by the massive generation of uranium-containing nuclear wastewater^{4,5}. In practical situations, the majority of uranium-containing nuclear wastewater is produced by the procedures of fuel production, such as uranium enrichment, uranium conversion, and fuel element fabrication, which requires the wide usage of uranium fluoride⁶. After the hydrolysis of uranium fluoride, the uranium in nuclear wastewater commonly exists in the form of uranyl (UO₂²⁺), together with the co-existing high concentration of fluoride ion (F⁻)⁷. As such, extracting uranium under the interference of high concentrations of F⁻ is an important issue for environmental protection and the recycling of uranium resources⁸⁻¹⁰. For this nuclear wastewater, the traditional adsorption or ion exchange method commonly requires the pre-precipitation of F⁻ by Ca²⁺, resulting in the formation of uranium-containing CaF₂ as radioactive solid waste^{11,12}. Accordingly,

searching for other technologies for uranium extraction is highly desired under the interference of high concentrations of F⁻.

As an emerging technology, electrochemical uranium extraction has attracted ever-increasing attention due to the fast kinetics, increased extraction capacity, and resistance to the interference of anions¹³⁻¹⁵. At present, electrochemical uranium extraction has been applied in the aqueous systems without F⁻^{16,17}. For example, the Fe-N_x-C single atoms with functional amidoxime groups¹⁸ were reported to achieve an extraction capacity of 1.2 mg g⁻¹ from real seawater over 24 h. However, despite the significant progress, the electrochemical uranium extraction in real nuclear wastewater with the existence of F⁻ is still challenging, because of the rather complex species of uranium due to the coordination effect^{19,20}. Specifically, the dominant hexavalent uranium (U(VI)) species generally lies on a series of uranyl fluoride (UO₂F_x)²¹, such as UO₂F⁺, UO₂F₂, and UO₂F₃⁻, instead of bare UO₂²⁺. In this case, the conventional uranium extraction sites suffer from the competing coordination of uranium and F⁻, thus resulting in the poor extraction efficiency

¹State Key Laboratory of Environment-friendly Energy Materials, School of National Defense, School of Life Science & Engineering, School of Materials & Chemistry, National Co-innovation Center for Nuclear Waste Disposal & Environmental Safety, Sichuan Civil-military Integration Institute, Southwest University of Science & Technology, Mianyang, P. R. China. ²School of Chemistry and Materials Science, Anhui Normal University, Wuhu, P. R. China.

✉ e-mail: ly0201@ahnu.edu.cn; zhuwenkun@swust.edu.cn; her@swust.edu.cn

of uranium under the interference of high concentrations of F^- . Therefore, the construction of specific sites for the binding of UO_2F_x is an essential prerequisite for achieving efficient electrochemical uranium extraction in real nuclear wastewater with high concentrations of F^- .

Herein, we develop the $Ti(OH)PO_4$ with $Ti^{\delta+}-PO_4^{3-}$ ion pair extraction sites for selective binding of UO_2F_x and efficient electrochemical uranium extraction under the interference of high concentration of F^- . Both synchrotron X-ray absorption fine structure (XAFS) and theoretical simulation demonstrate that the $Ti^{\delta+}-PO_4^{3-}$ ion pair extraction sites are strongly bound with UO_2F_x through the combined interactions of $Ti^{\delta+}-F^-$ and $PO_4^{3-}-UO_2^{2+}$. During the uranium extraction, the UO_2F_x is reduced to U_3O_7 as a gray deposit followed by further oxidation and crystallization as $K_3UO_2F_5$. In 400 mL of real nuclear wastewater produced by fuel production, the $Ti(OH)PO_4$ achieves an electrochemical extraction efficiency of 99.6% for uranium within 7 h, with an extraction capacity of 6829 mg g^{-1} without saturation. The uranium-containing powder is successfully collected from the real nuclear wastewater, with 92.1% of uranium proportion among the metal elements in the powder.

Results

Construction of $Ti(OH)PO_4$ with ion pair sites

The construction of ion pair sites originated from the reconstruction of lamellar OH-terminated Ti_3C_2 , as illustrated in Fig. 1a. Initially, the Al

layers of commercial bulk Ti_3AlC_2 were etched to form the accordion-like stack of F-terminated Ti_3C_2 nanosheets. Followed by the exfoliation process under N_2 protection in aqueous solution, the stacked F-terminated Ti_3C_2 nanosheets were transformed into lamellar OH-terminated Ti_3C_2 nanosheets (Supplementary Fig. 1). The flexible exfoliated lamellar OH-terminated Ti_3C_2 nanosheets were confirmed by the high-resolution transmission electron microscope (HRTEM) images, and the X-ray diffraction (XRD) pattern^{22–24} (Supplementary Fig. 2). As shown by Fourier transform infrared spectroscopy (FT-IR) measurement, the exfoliated lamellar OH-terminated Ti_3C_2 nanosheets lacked the peak of C-F stretching at 1080 cm^{-1} relative to accordion-like stacked Ti_3C_2 nanosheets, demonstrating the replacement of -F terminations by -OH terminations during the exfoliation process (Supplementary Fig. 3). After that, a wet chemical treatment was applied to transform the exfoliated lamellar OH-terminated Ti_3C_2 into $Ti(OH)PO_4$, which contained an ion pair of $Ti^{\delta+}$ ($\delta < 4$) and PO_4^{3-} . As shown by the transmission electron microscopy (TEM) images, the $Ti(OH)PO_4$ exhibited a nanorod-like morphology (Fig. 1b). The atomic force microscopy (AFM) analysis and the corresponding three-dimensional graph of $Ti(OH)PO_4$ nanorods indicated the narrow height distribution due to the regular stacking (Supplementary Fig. 4). Figure 1c showed the HRTEM image of a free-standing $Ti(OH)PO_4$ nanocrystal. The $Ti(OH)PO_4$ nanorod exhibited a periodic layer-by-layer structure with a

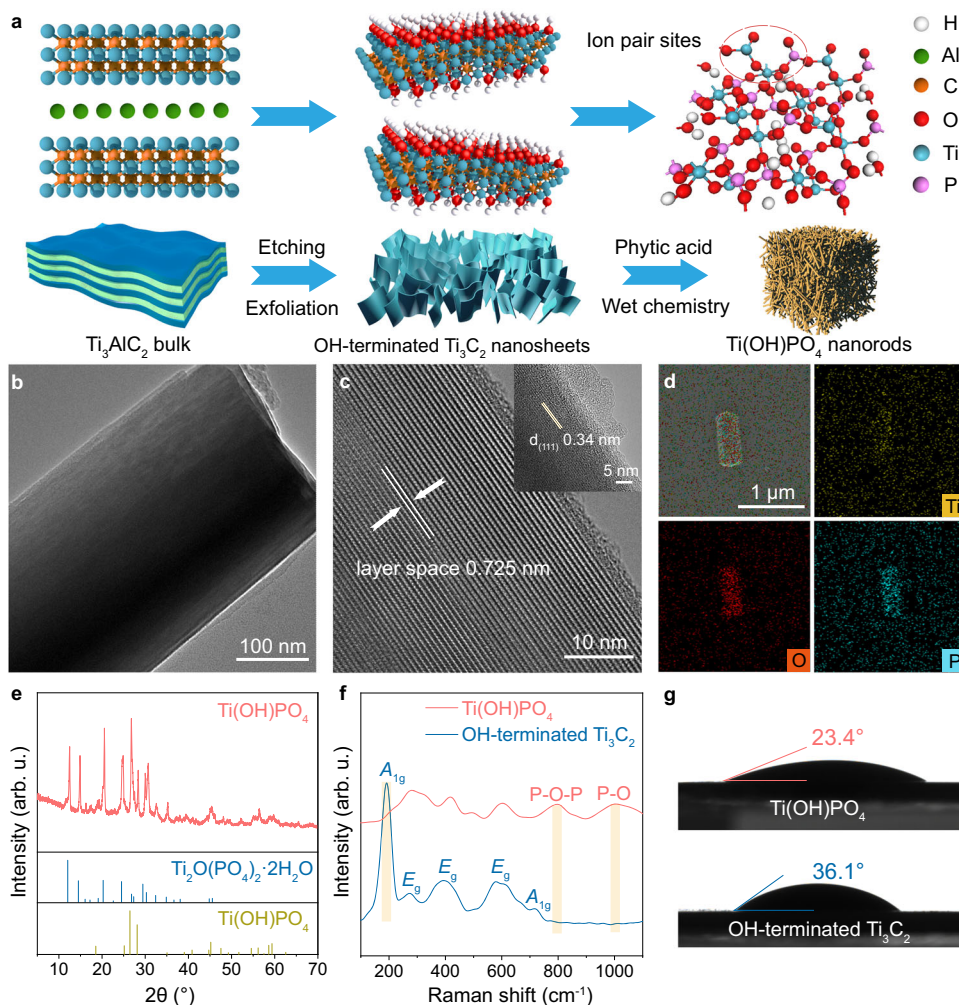


Fig. 1 | Construction of ion pair sites. **a** The schematic illustration for the preparation of the $Ti(OH)PO_4$ with ion pair sites. **b** TEM image of $Ti(OH)PO_4$ nanorods. **c** HRTEM image of $Ti(OH)PO_4$ nanorods. Inset: HRTEM image of the boundary of $Ti(OH)PO_4$ nanorods. **d** EDS analysis of $Ti(OH)PO_4$ nanorods. **e** XRD pattern, **f** Raman spectra, and **g** static contact angle of $Ti(OH)PO_4$ nanorods and lamellar

OH-terminated Ti_3C_2 nanosheets. The highlighted areas in Fig. 1f show the A_{1g} peak of OH-terminated Ti_3C_2 and the P-O-P and P-O peaks of $Ti(OH)PO_4$, respectively. Credits: **a** (schematic models) copyright Hangzhou SPHERE Technology Co., Ltd. Source data are provided as a Source Data file.

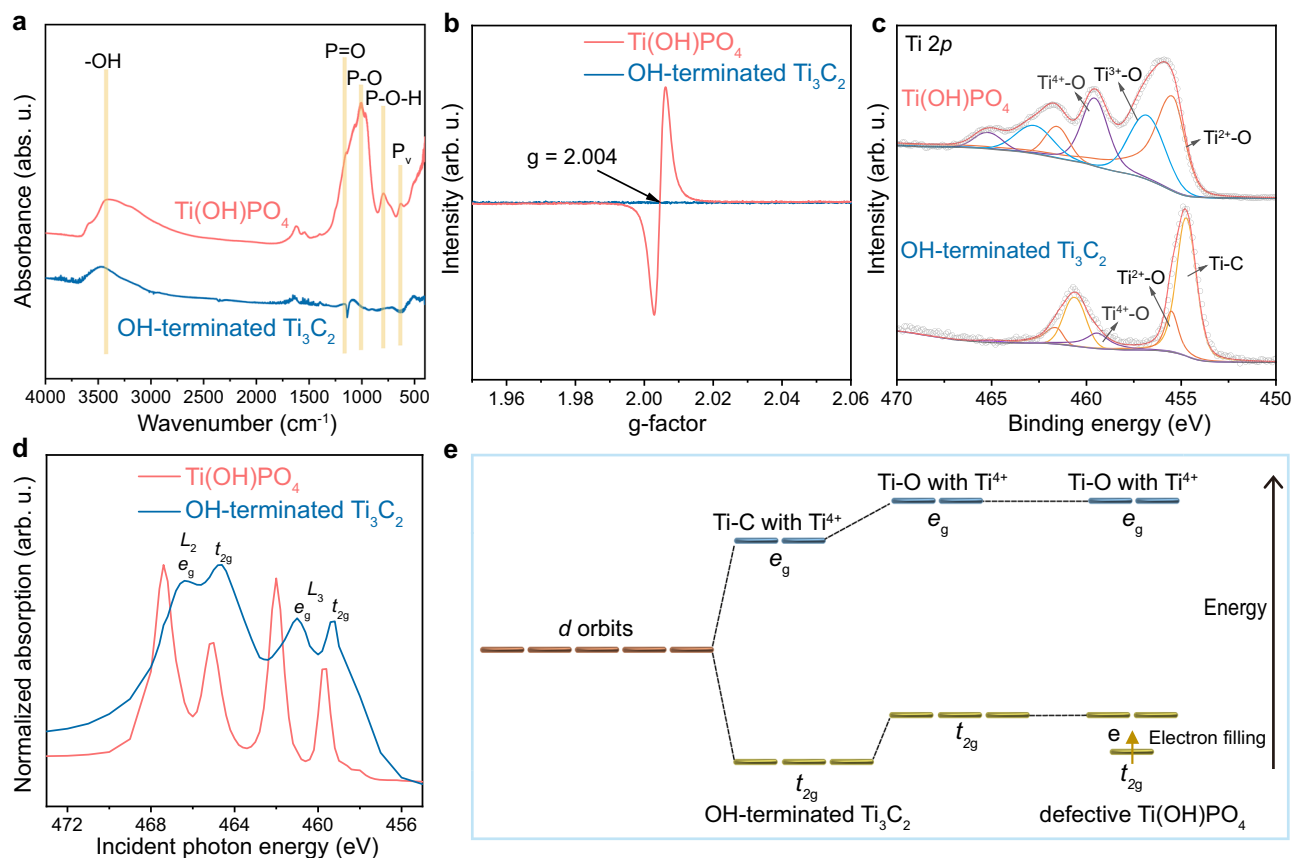


Fig. 2 | Bonding and electronic structure of ion pair sites. a FT-IR spectrum, **b** ESR spectrum, **c** Ti 2p XPS spectrum, and **d** XANES spectrum of Ti(OH)PO₄ nanorods and lamellar OH-terminated Ti₃C₂ nanosheets. **e** Energy diagram of the

splitting orbits of Ti 3d peak. *L*₂ and *L*₃ represent two different sub-energy levels in the *L* shell of the Ti atom, respectively. *e*_g and *t*_{2g} represent the energy level splitting of *d* orbitals in the coordination field. Source data are provided as a Source Data file.

spacing of 0.725 nm, which was larger than the diameter of uranyl or uranyl fluoride (<0.4 nm). The inset was the edge region of the rod structure, which displayed the lattice fringe with interlayer spacing of 0.34 nm and indicated the (111) facets of Ti(OH)PO₄. Determined by energy dispersive X-ray spectroscopy (EDS), the Ti, O, and P elements filled the outline of the selected region, indicating the uniform distribution of the elemental components in the Ti(OH)PO₄ nanorod (Fig. 1d).

The physical phase of Ti(OH)PO₄ nanorods was further validated. Two sets of diffraction peaks appeared in the XRD pattern of the Ti(OH)PO₄ nanorods (Fig. 1e). The two sets of characteristic peaks were identified as the standard monoclinic Ti(OH)PO₄ phase (JCPDS #36-0697) and Ti₂O(P₂O₇)₂·2H₂O (JCPDS #52-1529). Notably, the Ti₂O(P₂O₇)₂·2H₂O was the dimerization of Ti(OH)PO₄ after a dehydration process, indicating the transformable hydroxyl in Ti(OH)PO₄. Figure 1f shows the Raman spectra of Ti(OH)PO₄ and lamellar OH-terminated Ti₃C₂. After the reconstruction of OH-terminated Ti₃C₂ into Ti(OH)PO₄, the A_{1g} peak of pristine OH-terminated Ti₃C₂ disappeared, accompanied by the characteristic peaks of Ti-O bonds and P-O bonds^{25,26}. Moreover, the Ti(OH)PO₄ exhibited a water static contact angle of 23.4°, which was lower than that of pristine lamellar OH-terminated Ti₃C₂ (Fig. 1g). Such phenomenon resulted from the incorporation of hydroxyl into lattice with the enhanced hydrogen bonds in Ti(OH)PO₄, further demonstrating the existence form of Ti(OH)PO₄.

The ion pair sites in Ti(OH)PO₄ were investigated by the analysis of the bonding and electronic structure of Ti(OH)PO₄. Determined by FT-IR measurement (Fig. 2a), the stretching vibrations of P=O, P-O, and P-O-H in PO₄³⁻ group were observed in the spectrum of Ti(OH)PO₄, which differed from that of OH-terminated Ti₃C₂²⁷. In the electron spin

resonance (ESR) spectra (Fig. 2b), the Ti(OH)PO₄ exhibited a sharp resonance signal at the g-factor of 2.004, indicating the massive oxygen vacancies in Ti(OH)PO₄²⁸. Moreover, the X-ray photoelectron spectroscopy (XPS) analysis was performed to check the chemical bonds of Ti(OH)PO₄, which displayed the Ti, P, and O signals in the survey spectra (Supplementary Fig. 5a). The oxidative state of P in the PO₄³⁻ group was confirmed by the P 2p spectrum of Ti(OH)PO₄ (Supplementary Fig. 5b). In the O 1s spectrum, the peak of the O in the vicinity of oxygen vacancy was observed at 531.2 eV, further demonstrating the defective nature of Ti(OH)PO₄²⁹ (Supplementary Fig. 5c). Meanwhile, Ti₃C₂ possessed the dominant signal of Ti-C bond, together with the slight signal of Ti⁴⁺-O and Ti²⁺-O bonds, which was attributed to the -OH termination (Fig. 2c). By comparison, the Ti 2p spectrum of Ti(OH)PO₄ showed three sets of peaks, which were assigned as Ti⁴⁺-O, Ti³⁺-O, and Ti²⁺-O³⁰⁻³². The massive low valent Ti⁶⁺ ($\delta < 4$) indicated the defective nature of Ti(OH)PO₄, which was constructed by the oxygen vacancies during the transformation of OH-terminated Ti₃C₂ into Ti(OH)PO₄.

To further demonstrate the electronic structure of Ti in Ti(OH)PO₄ nanorods, we tested the *L*-edge X-ray absorption near-edge structure (XANES) spectra of hydroxyl-terminated Ti₃C₂ and Ti(OH)PO₄. As shown in Fig. 2d, both the *L*₂ edge and *L*₃ edge of Ti(OH)PO₄ nanorods exhibited a slight shift of 2*p* to *t*_{2g} transition and a dramatic shift of 2*p* to *e*_g transition relative to pristine OH-terminated Ti₃C₂. This result was illustrated by the energy diagram of the splitting orbits of the Ti 3*d* peak³³ (Fig. 2e). Typically, Ti possessed five 3*d* orbitals, which could be divided into two *e*_g orbitals and three *t*_{2g} orbitals^{34,35}. The binding energy of *e*_g and *t*_{2g} orbitals was associated with two factors, including the coordination environment and the electron filling of Ti. For the coordination environment, the transformation of Ti-C in

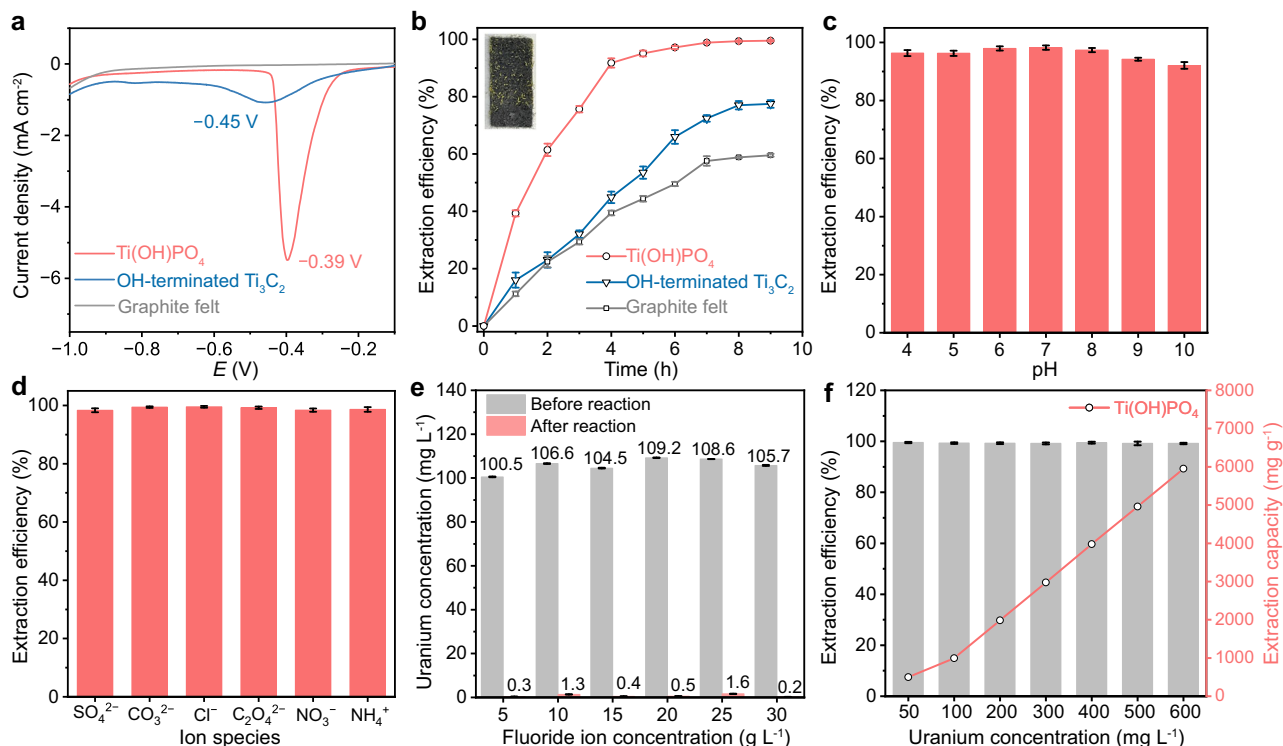


Fig. 3 | Electrochemical uranium extraction of ion pair sites. a LSV tests on Ti(OH)PO₄, OH-terminated Ti₃C₂, and bare graphite felt electrodes. *E* represents potential. **b** The electrochemical extraction efficiency of U(VI) on Ti(OH)PO₄, OH-terminated Ti₃C₂, and bare graphite felt electrodes. Inset: macroscopic deposition stripes of crystalline uranium. The stability of electrochemical extraction of U(VI) on Ti(OH)PO₄ electrode **c** under different pH conditions, **d** with different co-

existing ionic species. **e** The change in uranium concentration after electrochemical uranium extraction under electrolytes with different F⁻ concentrations (ranging from 5 g L⁻¹ to 30 g L⁻¹). **f** The electrochemical extraction efficiency of U(VI) on Ti(OH)PO₄ as the initial concentration of U(VI) varied from 50 mg L⁻¹ to 600 mg L⁻¹. Error bars represent standard deviation of three measurements. Source data are provided as a Source Data file.

OH-terminated T₃C₂ into Ti-O in Ti(OH)PO₄ induced the positive shift of both *e_g* and *t_{2g}* orbitals in Ti *L*-edge XANES, owing to the higher electronegativity of O than that of C. Moreover, for the factor of electron filling, Ti⁴⁺ possessed empty *e_g* and *t_{2g}* orbitals, whereas defective Ti(OH)PO₄ possessed abundant Ti³⁺ and Ti²⁺, which respectively had one and two electrons in 3*d* orbitals. Due to the lower energy of *t_{2g}* orbitals than *e_g* orbitals, the additional electrons in Ti^{δ+} were located at *t_{2g}* orbitals, resulting in the dramatic energy decrease of *t_{2g}* orbitals. As a comprehensive result of the coordination environment and the electron filling of Ti, the *e_g* peak in Ti(OH)PO₄ showed an obvious shift, whereas *t_{2g}* peak displayed a negligible shift relative to OH-terminated T₃C₂ in Ti *L*-edge XANES (Supplementary Table 1). The Ti^{δ+} and the PO₄³⁻ group in Ti(OH)PO₄ constructed the ion pair sites, which were the key species for the uranium extraction under the interference of high concentration of F⁻.

Electrochemical uranium extraction

The Ti(OH)PO₄ nanorods were uniformly spread on graphite felt to evaluate the effect of ion pair sites on the electrochemical uranium extraction. An aqueous solution containing 100 mg L⁻¹ of U(VI) and 30 g L⁻¹ of F⁻ was adopted as the electrolyte to simulate the wastewater of nuclear production. We demonstrated the reduction peak of U(VI) in this electrolyte by linear sweep voltammetry (LSV) test (Fig. 3a). The Ti(OH)PO₄ nanorods exhibited a sharp reduction peak at -0.39 V vs. Ag/AgCl, which corresponded to the reduction of U(VI) into pentavalent uranium (U(V)). By comparison, these peaks of pristine OH-terminated T₃C₂ and the bare graphite felt were located at more negative positions with rather weak intensity. To double-check the origin of the reduction peak, we performed Cyclic Voltammetry (CV) tests in the presence or absence of U(VI) in 30 g L⁻¹ of F⁻ (Supplementary Fig. 6). The overall current density of the CV curve

dramatically increased after the addition of U(VI), indicating that the U(VI) participated in the composition of double-layer capacitance³⁶. Besides, the reduction peak disappeared in the absence of U(VI), further demonstrating the ascription of the uranium reduction peak. These results indicated the Ti(OH)PO₄ nanorods possessed a special activity for uranium extraction in the presence of F⁻.

As shown in Fig. 3b, the electrochemical extraction efficiency of U(VI) on Ti(OH)PO₄ was 95.1% within 5 h, which was significantly superior to that of OH-terminated T₃C₂ (53.5%) and that of bare graphite felt (44.4%). Further discussion on the termination group of Ti₃C₂ indicated the -OH group was the extraction site, instead of -F (Supplementary Fig. 7 and Supplementary Table 2). Notably, the ultimate extraction efficiency of U(VI) from Ti(OH)PO₄ attained 99.5%, which enabled the direct observation of macroscopic deposition stripes of crystalline uranium (inset of Fig. 3b). In addition, compared with the non-voltage adsorption method, the electrochemical extraction efficiency of U(VI) on Ti(OH)PO₄ nanorods exhibited a 2-fold enhancement (Supplementary Fig. 8). To collect the uranium from the electrode, 0.1 mol of HCl solution was taken as the desorbing agent. After 10 seconds of washing time, the yellow stripe-like crystallization on the surface of the electrode gradually dispersed in the desorbing solution (Supplementary Fig. 9). As a result, the electrochemical method with Ti(OH)PO₄ as an electrode represented an efficient protocol for uranium extraction in the presence of a high concentration of F⁻.

The stability of electrochemical extraction of U(VI) on the Ti(OH)PO₄ nanorods was further evaluated. After 5 cycles of uranium extraction, the extraction efficiency of U(VI) on Ti(OH)PO₄ retained a high value of 92.2% (Supplementary Fig. 10). Moreover, regardless of the wide manipulation of pH from 4 to 10, the extraction efficiency of U(VI) on Ti(OH)PO₄ exceeded 90% (Fig. 3c). Furthermore, the

anti-interference capability of $\text{Ti}(\text{OH})\text{PO}_4$ was demonstrated by extraction efficiency in the presence of co-existing ions, especially SO_4^{2-} , CO_3^{2-} , Cl^- , $\text{C}_2\text{O}_4^{2-}$, NO_3^- , and NH_4^+ , which commonly existed in the wastewater of nuclear production (Fig. 3d). We also tested the changes in pH and ion concentrations before and after the electrochemical uranium extraction reaction (Supplementary Fig. 11). All the pH values of the electrolyte increased after the electrochemical reaction because of the hydrogen evolution in the electrochemical process. The extraction efficiency of U(VI) remained at a high level of >98%, indicating that none of the interference ions exhibited obvious influence on the U(VI) extraction. Moreover, the concentrations of anions in the electrolyte displayed a negligible decrease after the electrochemical reaction, which was attributed to the slight adsorption of ions by the electrode. We also evaluated the influence of F^- concentration change on uranium recovery (Fig. 3e). Regardless of the initial concentration of F^- , the U(VI) concentration was reduced from approximately 100 mg L^{-1} to 1 mg L^{-1} after the reaction with a high level of >98%, indicating that the F^- concentrations did not exhibit an obvious influence on the U(VI) extraction for the $\text{Ti}(\text{OH})\text{PO}_4$ electrode (Supplementary Fig. 12a). Such a phenomenon was attributed to the selective binding of UO_2F_x by ion pair sites, instead of UO_2^{2+} . Furthermore, slight decreases in the concentration of F^- were observed after the electrochemical reaction, which was ascribed to the adsorption by the Ti^{8+} cation site and further co-crystallization by the uranium product (Supplementary Fig. 12b). Moreover, as the initial concentration of U(VI) varied from 50 mg L^{-1} to 600 mg L^{-1} , the extraction efficiency of U(VI) by $\text{Ti}(\text{OH})\text{PO}_4$ remained consistently above 99%, indicating an extraction capacity of 5950 mg g^{-1} without the phenomenon of extraction saturation (Fig. 3f). These results suggested the potential use of $\text{Ti}(\text{OH})\text{PO}_4$ with ion pair sites towards the electrochemical uranium extraction in the wastewater of nuclear production.

Evolution of uranium species

The effective electrochemical uranium extraction of $\text{Ti}(\text{OH})\text{PO}_4$ nanorods with ion pair sites in the presence of high concentrations of F^- inspired us to explore the process of uranium deposition on the electrode. The time-dependent extraction experiment on $\text{Ti}(\text{OH})\text{PO}_4$ nanorods was conducted in an aqueous electrolyte containing 600 mg L^{-1} of U(VI) and 30 g L^{-1} of F^- (Fig. 4a). At the time point of 1 h, the deposited species appeared and exhibited a gray color. With the reaction proceeding to 3 h and 5 h, the gray deposit was gradually transformed into the yellow product, together with the aggregation of the solid deposits on the electrode. The color of the deposit finally transformed to a stable state of deep yellow at 7 h. To validate the species during the uranium extraction, we collected the solid deposits at different time points. As indicated by XRD patterns, the gray deposits at 1 h and 3 h were ascribed to U_3O_7 (JCPDS #42-1215), which was a special species of UO_{2+x} containing U(V) and tetravalent uranium (U(IV)) (Fig. 4b). The existence of U(IV) can be explained by the dismutation of U(V). By comparison, the XRD of yellow deposits at 5 h and 7 h well fitted by $\text{K}_3\text{UO}_2\text{F}_5$ (JCPDS #38-0023) with domain species of U(VI), indicating the oxidation of low valent uranium in the deposits during the reaction. The $\text{K}_3\text{UO}_2\text{F}_5$ species was also responsible for the slight decreases in the concentration of F^- in the experiment of Supplementary Fig. 12. The K in the final uranium extraction product ($\text{K}_3\text{UO}_2\text{F}_5$) originated from the KF in the electrolyte, which could be replaced by Na in $\text{Na}_3\text{UO}_2\text{F}_5$ when using NaF as electrolyte (Supplementary Fig. 13).

The result of uranium evolution was verified by the U 4f XPS spectra at different time points (Fig. 4c). With the reaction proceeding to 3 h, the peaks of U 4f_{7/2} were negatively shifted from 381.5 eV to 380.7 eV, indicating the continuous reduction of uranium during the reaction. With the reaction proceeding to 4 h and 7 h, the gray deposit was gradually transformed into the yellow product, together with the peaks of U 4f_{7/2} positively shifted to 381.8 eV, indicating the oxidation

of low valent uranium in the deposits during the reaction^{37,38}. For a precise interpretation, the gray deposits possessed more content of U(IV) and U(V) than that of the yellow deposits (Supplementary Fig. 14). The intermediate of U_3O_7 and final product of $\text{K}_3\text{UO}_2\text{F}_5$ were also observed through the deposits of multiple cycles of CV test, which verified the evolution process of uranium species (Supplementary Fig. 15). The alternation of the uranium species in the deposit was accompanied by the shape evolution. At a reaction time of 1 h, the initial gray uranium deposits displayed a nanoneedle morphology with low crystallization (Supplementary Fig. 16). As time proceeded, the nanoneedles gradually evolved into nanosheets, with visible crystalline lattice fringes. Figure 4d showed a typical TEM image of the final yellow deposits, which showed the flexible nanosheet morphology. Moreover, the lattice fringes of this nanosheet possessed the interplanar spacing of 0.32 nm, belonging to the (220) facet of $\text{K}_3\text{UO}_2\text{F}_5$ (Fig. 4e). In the EDS measurement, the U, K, and F elements were uniformly distributed in the nanosheets, further demonstrating the composition of the $\text{K}_3\text{UO}_2\text{F}_5$ in the final yellow deposits (Fig. 4f). Accompanied by the shape evolution of the uranium deposit, the morphology of $\text{Ti}(\text{OH})\text{PO}_4$ transformed from pristine stacked nanosheets to exfoliated nanosheets through the expansion of interlayer spacing (Supplementary Fig. 17). This result demonstrated the uranyl intercalation into the interlayer spaces of $\text{Ti}(\text{OH})\text{PO}_4$ during the electrochemical reaction, which verified the advantage of larger interlayer spacing of $\text{Ti}(\text{OH})\text{PO}_4$ than the diameter of UO_2F_x .

To validate the species evolution involved in the uranium extraction, we directly investigated the valence state and coordination environment of uranium in the electrode at 3 h during the electrochemical reaction. Notably, the key intermediate deposit was not separated from the extraction material in this case. As shown by the U $L_{3\text{-edge}}$ XANES spectra (Fig. 4g), the characteristic peaks at 17175.7 eV in the spectrum were identified as the white line peak, corresponding to the transition of electrons from the occupied U 2p orbital to the unoccupied U 6d³⁹. Significantly, the absorption edge position of electrochemical products was situated between $\text{UO}_2(\text{NO}_3)_2$ and U_3O_8 , with a slight shift towards the low-E side. This observation implied that the valence states of U cations encompassed a range between +4 and +6, indicating the uranium extraction underwent the electrochemical reduction process. Figure 4h illustrated the Fourier transform (FT) k^2 -weighted extended X-ray absorption fine structure (EXAFS) spectra of the electrochemical product. The FT curve of the electrochemical product had two main peaks at 1.4 and 1.9 Å, which were attributed to the U-O coordination of the first and second shells⁴⁰. The first and second shells were denoted as U-O_{ax} and U-O_{eq}, which respectively referred to the axial O of uranyl species and the O atom at the adsorption site of ion pair sites. Through the EXAFS fitting, the coordination numbers of U-O_{ax} and U-O_{eq} were 2.2 and 3.4, respectively (Fig. 4i and Table 1). This result suggested that the adsorption process was assisted by three O atoms in the surface ion pair sites of $\text{Ti}(\text{OH})\text{PO}_4$ nanorods. Specially, the U-F bond co-existed with a coordination number of 1.1, demonstrating the target adsorbate involved in the uranium extraction was the overall UO_2F_x instead of UO_2^{2+} , which resulted from the Coulomb interaction between ion pair sites and UO_2F_x .

Reaction mechanism

The unusual adsorption of the overall UO_2F_x and the corresponding species evolution motivate us to explore the intrinsic reaction mechanism. Based on the species evolution, we constructed a scheme to simulate the reaction process (Fig. 5a). The UO_2F_x was adsorbed on the ion pair sites of $\text{Ti}(\text{OH})\text{PO}_4$ nanorods without the separation of the U-F bond. After that, the uranyl was reduced to low-valent species, which weakened the Coulombian force of uranyl and F^- , thus resulting in the formation of an intermediate UO_{2+x} product. The metastable low-valent uranium was then oxidized, followed by crystallizing with F^- and forming the final $\text{K}_3\text{UO}_2\text{F}_5$.

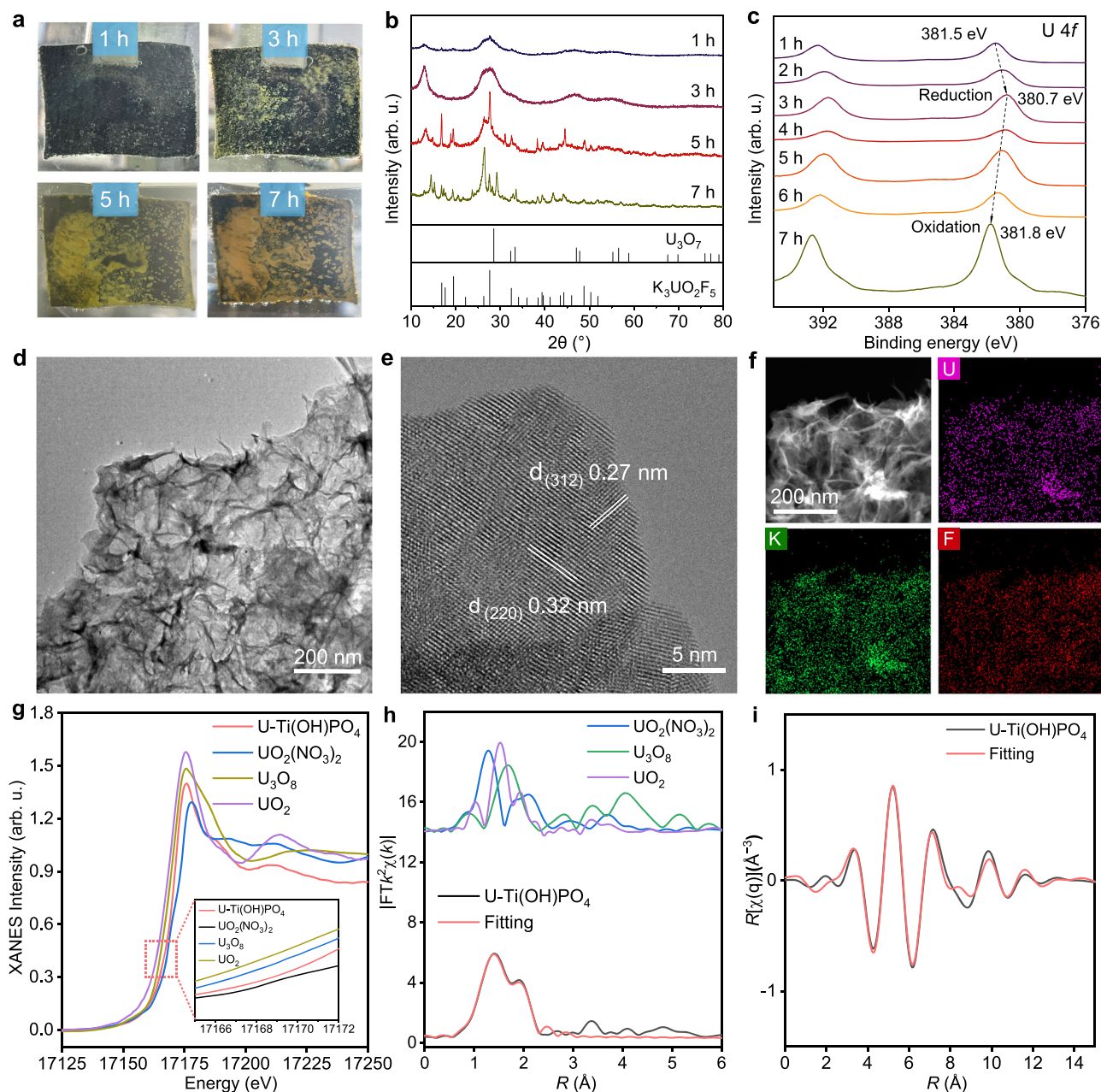


Fig. 4 | Evolution of uranium species. **a** Photographs of the evolution of uranium species during the uranium extraction. **b** XRD pattern of the collected solid deposits at different time points. **c** U 4f XPS spectrum of U-Ti(OH)PO₄ electrodes at different electrochemical extraction time points. **d** TEM image of the final yellow deposits with nanosheet morphology. **e** HRTEM and **f** EDS measurement of the

composition of the K₃UO₂F₅ in the final yellow deposits. **g** The U L₃-edge XANES spectra of intermediate deposit. Inset: magnified pre-edge XANES region. **h** The FT k²-weighted EXAFS spectra of the electrochemical product. **i** The corresponding k-space fitting curves of the electrochemical product. Source data are provided as a Source Data file.

Considering the adsorption of the overall UO_{2+x} was the key factor that influenced the extraction efficiency of uranium, we theoretically simulated the adsorption of UO₂F_x on the ion pair site of Ti(OH)PO₄ nanorods (Fig. 5b, Supplementary Table 3, and Supplementary Data 1).

Table 1 | Structural parameters of U-Ti(OH)PO₄ at the U L₃-edge extracted from quantitative EXAFS curve-fittings

Path	CN	R (Å)	σ ² (10 ⁻³ Å ²)	ΔE (eV)	R-factor
U-O _{ax}	2.2	1.7	4.1	-11.1	0.004
U-O _{eq}	3.4	2.3	4.0	6.8	0.004
U-F	1.1	2.1	5.0	-11.0	0.004

Taking UO₂F⁺ as an example, we compared the optimized adsorption configuration on OH-terminated Ti₃C₂ and Ti(OH)PO₄ with Ti⁶⁺ on the surface. The OH-terminated Ti₃C₂ possessed the normal -OH sites for bare UO₂²⁺ adsorption, which possessed adsorption energy of -2.6 eV for UO₂F⁺ without the interaction of F⁻ and Ti⁴⁺. For the Ti(OH)PO₄ model, the coordination of surface Ti⁶⁺ was unsaturated, giving rise to the interaction with F⁻. As such, the UO₂F⁺ has stabilized on the PO₄³⁻-Ti⁶⁺ ion pair sites through both the PO₄³⁻-UO₂²⁺ and Ti⁶⁺-F⁻ interactions. In this model, three O atoms in the Ti(OH)PO₄ participated in the adsorption of UO₂F⁺, consistent with the experimental EXAFS result. Moreover, the adsorption energy of UO₂F⁺ on the ion pair sites of Ti(OH)PO₄ was -4.5 eV, which was much more negative than that on the -OH sites of OH-terminated Ti₃C₂. The adsorption energy was able to be

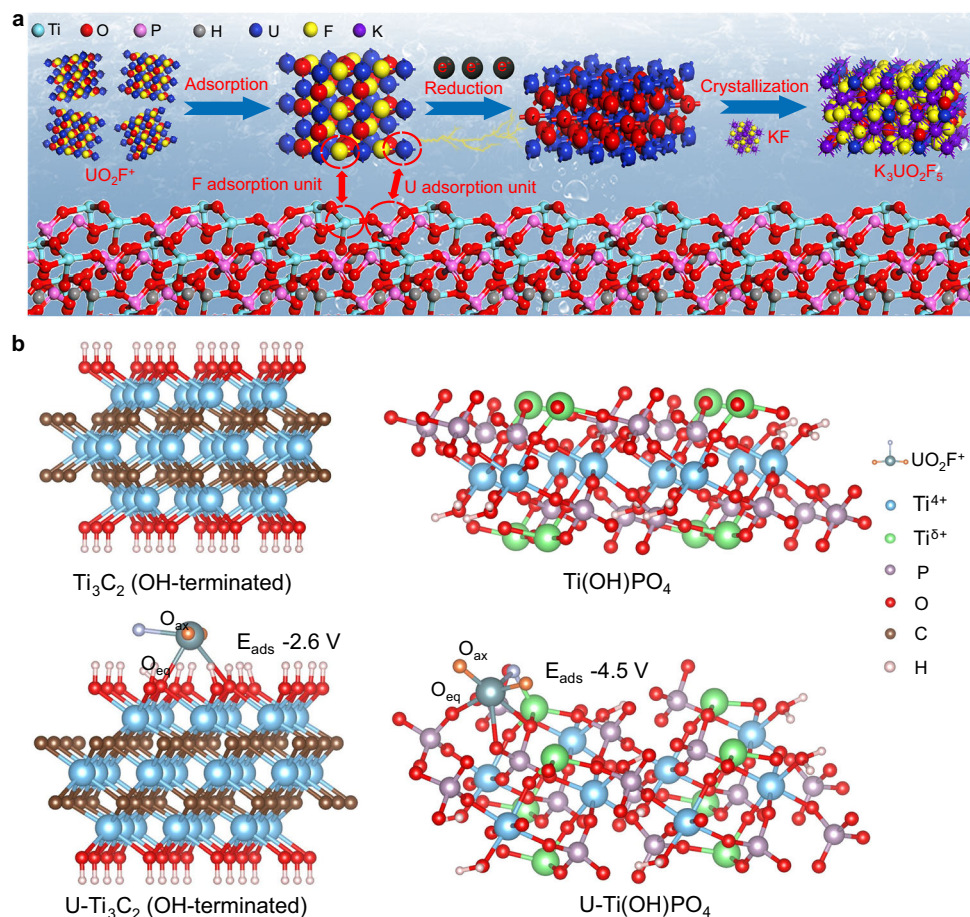


Fig. 5 | Reaction mechanism of ion pair sites. **a** The schematic diagram of the rational reaction mechanism of Ti(OH)PO_4 ion pair sites. **b** Optimized adsorption configurations of UO_2F^+ adsorbed on the Ti_3C_2 (OH-terminated) and

Ti(OH)PO_4 . O_{ax} the axial O of uranyl species, O_{eq} the O atom at the adsorption site, E_{ads} the adsorption energy of UO_2F^+ . Source data are provided as a Source Data file.

further decreased by introducing additional O vacancies (Supplementary Fig. 18). Furthermore, the bond angle of $\text{O}_{\text{ax}}\text{-U-O}_{\text{ax}}$ of $\text{UO}_2\text{F}^+\text{-Ti(OH)PO}_4$ model was 100.6° , which was lower than that (167.4°) of $\text{UO}_2\text{F}^+\text{-Ti}_3\text{C}_2$ (OH-terminated). Given that the reduction of UO_2^{2+} requires the decrease of bond angle, the ion pair sites of Ti(OH)PO_4 can facilitate the reduction of UO_2^{2+} in UO_2F^+ . As a result, the ion pair sites stabilized the adsorption of UO_2F_x and promoted the reduction of UO_2^{2+} , which was responsible for the uranium extraction in high concentrations of F^- .

Experiment of real nuclear wastewater

Motivated by the distinctive effect of ion pair sites on the uranium extraction in high concentrations of F^- , we explored the uranium extraction from real nuclear wastewater on Ti(OH)PO_4 . This wastewater consisted of high levels of F^- (8 g L^{-1}), CO_3^{2-} (5.5 g L^{-1}), HCO_3^- (4.5 g L^{-1}), NO_3^- (3 g L^{-1}), Cl^- (2 g L^{-1}), NH_4^+ (3 g L^{-1}), and $\text{C}_2\text{O}_4^{2-}$ (5 g L^{-1}), which was produced by the washing of container in a nuclear fuel production facility. After 7-h electrolysis at a constant current density of 30 mA cm^{-2} , the concentration of U(VI) was reduced from an initial value of 685.1 mg L^{-1} to 2.2 mg L^{-1} , with 99.6% of extraction efficiency and 6829 mg g^{-1} of extraction capacity (Fig. 6a). Such value of extraction efficiency was 1.7-time larger relative to that of OH-terminated Ti_3C_2 (55.9%), indicating the effectiveness of Ti(OH)PO_4 with ion pair sites (Supplementary Fig. 19). With the proceeding of the electrolysis, the yellow color of real wastewater gradually faded, finally resulting in a colorless and transparent residual liquid (Fig. 6b). The concentration of all metal species in the transparent residual liquid was displayed in the Supplementary Table 4. Compared with the yellow real

wastewater, the K^+ and Na^+ respectively decreased by 697.3 mg L^{-1} (0.5% decrease) and 136.6 mg L^{-1} (2.2% decrease), which was mainly ascribed to the adsorption of the electrode, instead of the electrochemical extraction (Supplementary Fig. 20). The majority of adsorbed Na^+ and K^+ could be removed from the electrode by washing process. Additionally, the low initial concentrations (below 2 mg L^{-1}) of trace metal elements were essentially inconsequential to the uranium extraction process and purity of uranium deposits. Therefore, the uranium was able to be efficiently extracted from the electrode.

After the electrochemical reaction, the uranium was densely deposited on the electrode, which can be desorbed, simply precipitated by KOH, and collected as a solid powder (Fig. 6c). We analyzed the proportion of metal species in this powder by inductively coupled plasma optical emission spectrometry (ICP-OES) measurement (Fig. 6d). The proportion of uranium reached 92.1% among the metal elements in the powder, which was convenient for the following separation and reuse of uranium. In addition, we employed a typical precipitation-calcination process for the further purification of uranium products (Fig. 6e). Initially, we collected and dissolved uranium extraction product in HCl. Subsequently, excess ammonia was added to the above solution to form a precipitate of ammonium diuranate. Finally, ammonium diuranate was collected by centrifugation and heated at 550°C for 5 h to form a black-green uranium product. According to XRD (Supplementary Fig. 21) and ICP-OES tests (Fig. 6f), the purified black-green uranium product was identified as U_3O_8 (JCPDS #31-1425) with a uranium content of 99.93% among the metal elements, which can be directly used in the uranium production.

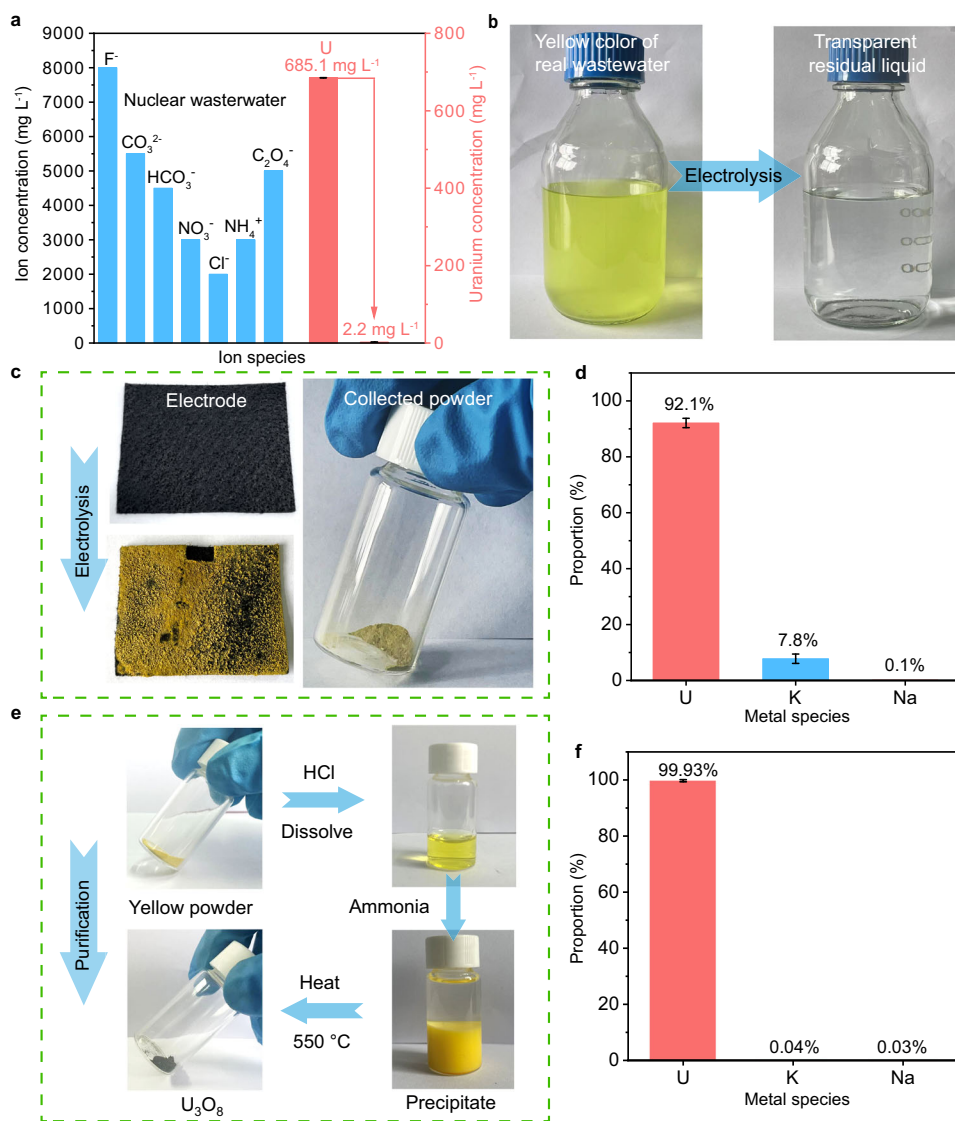


Fig. 6 | Experiment of real nuclear wastewater of ion pair sites. a The electrochemical extraction efficiency of U(VI) on Ti(OH)PO₄ in real nuclear wastewater. **b** The color change of real nuclear wastewater before and after electrolysis. **c** The deposited uranium on the electrode and the corresponding collected powder after electrolysis. **d** The proportion of uranium among the metal species in the powder.

e The schematic diagram of the precipitation-calcination purification process for uranium. **f** The proportion of uranium among the metal species in the purification product. Error bars represent standard deviation of three measurements. Source data are provided as a Source Data file.

Consequently, the electrochemical uranium extraction by Ti(OH)PO₄ provided a feasible strategy for resource recovery in real wastewater of nuclear production. We also evaluated the approximate operating cost. The consumed electricity was 31.5 Wh, which means the extraction per kg of U requires electricity of -115 kWh, corresponding to an electricity cost of -8 US dollars (according to the price of China). For the cost of Ti(OH)PO₄ electrode, the price was approximately 0.2 US dollars considering the purchase of Ti₃AlC₂ precursor, synthetic material, and graphite support. Considering the recycling use of the electrode, the cost of electrode material was -14 US dollars for extracting 1 kg of uranium. Therefore, the overall cost was approximately 22 US dollars for the extraction of 1 kg U considering both energy consumption and material costs.

Discussion

In summary, the Ti⁶⁺-PO₄³⁻ ion pair sites are constructed in Ti(OH)PO₄ as uranium extraction material for nuclear wastewater containing high concentrations of F⁻ from fuel production. In simulated electrolytes with

up to 30 g L⁻¹ of F⁻, Ti(OH)PO₄ possesses an extraction efficiency of 95.1% in 5 h. The mechanistic study reveals that UO₂F_x can be strongly bound in the form of 2O_{ax}-U-3O_{eq} and Ti-F bonds. With the reaction proceeding, the adsorbed UO₂F_x is transformed from the reduced state (U₃O₇) to the crystalline state (K₃UO₂F₅). In a real nuclear wastewater experiment, the Ti(OH)PO₄ exhibits 99.6% extraction efficiency of uranium within 7 h regardless of the interferential 8 g L⁻¹ of F⁻, with an extraction capacity of 6829 mg g⁻¹ without saturation. After the simple collection, the powder product containing high-purity of uranium is obtained, demonstrating the successful recycling of uranium in real wastewater. Our work not only presents an efficient uranium extraction material for resisting high concentrations of F⁻, but also provides an efficient strategy for uranium recovery in real and complex nuclear wastewater.

Methods

Chemicals and materials

Ti₃AlC₂ powder (400 mesh) was purchased from 11 Technology Co., Ltd. Hydrochloric acid (HCl, ≥ 36% purity) and Phytic acid (PA, 70%

purity) were supplied by Chengdu Kelong Chemical Factory. Lithium fluoride (LiF, 99% purity) and Uranium nitrate ($\text{UO}_2(\text{NO}_3)_2 \cdot 6\text{H}_2\text{O}$, 99% purity) were obtained from Aladdin Shanghai Chemical. Graphite felt (Carbon content $\geq 99\%$) and ethanol (AR) were purchased from CeTech Co., Ltd. Nafion membrane solution (NRSO, 5 wt%) was acquired from Shanghai Macklin Biochemical Co., Ltd. The real nuclear wastewater was collected from a nuclear fuel production facility. All reagents and solvents were used without purification.

Characterizations

Scanning electron microscopy (SEM) images were displayed on a JSM-7800F Scanning Electron Microscope. Transmission electron microscopy (TEM), high-resolution transition electron microscopy (HRTEM), and energy dispersive X-ray spectroscopy (EDS) images were displayed on a JEM 2100 F transmission electron microscope operating at an accelerating voltage of 200 kV. Atomic force microscopy (AFM) images were obtained on a Bruker Dimension ICON testing at ScanAsyt mode. Inductively coupled plasma optical emission spectrometry (ICP-OES) analyses were performed on PerkinElmer ICP 2100 and PerkinElmer Optima 5300 DV. X-ray diffraction (XRD) data were collected on a Smartlab SE diffractometer equipped with a $\text{Cu K}\alpha$ source. Raman spectra (Raman) were obtained on a Thermo Fischer DXR Laser Raman spectrometer testing at a wavelength of 532 nm. Fourier transform infrared (FT-IR) spectroscopy was determined from Nicolet iS 10 Spectrometer. The defects and surface properties of materials were identified by electron spin resonance (ESR) spectroscopy using a Bruker EMXplus. X-ray photoelectron spectroscopy (XPS) analysis was performed through Thermo Kalpha, equipped with a monochromatic $\text{Al K}\alpha$ X-ray source. The concentration of anions in the electrolyte was determined by an ion chromatograph (IC). The oxidation states characterization of the samples was utilized by the X-ray absorption fine structure (XAFS) through the transmission mode for Ti L edge and U L_{3} -edge in the National Synchrotron Radiation Laboratory (NSNR). The absorption edge positions were calibrated during the XAFS measurements. Extended X-ray absorption fine structure (EXAFS) data were collected from the ATHENA module, integrated within the IFEFIT software suite. Linear sweep voltammetry (LSV) and Cyclic Voltammetry (CV) data were displayed on the CHI 660E electrochemistry workstation.

Theoretical calculations

We have performed the DFT calculations in our system by using the Vienna ab initio simulation package (VASP, Version: VASP 5.4.4)^{41,42}. The PBE function was used for describing electronic exchange⁴³. The projector augmented wave method was adopted to describe the interactions between the ion cores and valence electrons^{44,45}. The energy cutoff for the plane-wave basis set was 500 eV. The Brillouin scheme sampled the Monkhorst-Pack scheme using a $3 \times 3 \times 1$ k-point grid⁴⁶. During the geometry optimization and electronic structure calculation, the atomic positions were optimized until the energy and the maximum force were $<10^{-5}$ eV atom^{-1} and 0.02 eV \AA^{-1} , respectively. The van der Waals dispersion by employing the DFT-D3 method of Grimme was considered for all the calculations⁴⁷.

Construction of $\text{Ti}(\text{OH})\text{PO}_4$ with ion pair sites

The exfoliated lamellar OH-terminated Ti_3C_2 nanosheets were synthesized following the MILD method by in situ HF selective etching of the Al layer of Ti_3AlC_2 precursor. Specifically, LiF (3.20 g) was dissolved with HCl (12.0 M, 40 mL) solution in a Teflon beaker, followed by the slow addition of Ti_3AlC_2 (2.00 g) in an ice bath under magnetic stirring. The reaction was conducted at 40 °C under ventilated conditions for 24 h to avoid safety hazards caused by HF use. The accordion-like stack -F-terminated Ti_3C_2 was collected and centrifuged at $2515 \times g$ several times with deionized water to remove any vestigial acid until the supernatant reached a pH of 6. Subsequently, the slurry above was

immersed in deionized water (100 mL) to form a homogeneous suspension via sonication for 2 h under the protection of N_2 . After that, the exfoliated OH-terminated $\text{Ti}_3\text{C}_2\text{T}_x$ aqueous supernatant in a centrifuge tube was collected after centrifugation once again at $1760 \times g$ for 5 mins. Finally, the suspension for the experiments was prepared by diluting the exfoliated OH-terminated $\text{Ti}_3\text{C}_2\text{T}_x$ suspension to 20 mg mL^{-1} . The $\text{Ti}(\text{OH})\text{PO}_4$ ion pair sites were synthesized via a facile wet chemical method. Typically, the exfoliated OH-terminated $\text{Ti}_3\text{C}_2\text{T}_x$ suspension (2 mL) was mixed with deionized water (40 mL) and stirred for 30 mins at room temperature to obtain a uniformly dispersed solution. Then, phytic acid (1.6 mL) was added to the above-dispersed solution dropwise and kept stirring for another 1 h. Afterward, the homogeneous solution was placed into a Teflon-lined autoclave (50 mL) and heated at 180 °C for 12 h. Finally, the $\text{Ti}(\text{OH})\text{PO}_4$ ion pair sites were collected after washing with deionized water and ethanol several times, and freeze-dried for 24 h.

Electrochemical uranium extraction experiments in simulated nuclear wastewater

The electrochemical uranium extraction experiments in simulating nuclear wastewater were measured with a three-electrode system. The working electrodes were fabricated as follows: $\text{Ti}(\text{OH})\text{PO}_4$ ion pair sites (5.00 mg), carbon black (2.00 mg), and Nafion Membrane solution (20 μL) were mixed with ethanol (2 mL) and sonicated until they became a homogeneous ink. The as-prepared ink was directly brush-coated on graphite felt (1 cm \times 1 cm) and dried at 80 °C. The platinum (Pt) wire and Ag/AgCl electrode were used as the counter electrode and reference electrode, respectively. The uranium extraction experiments were conducted under a constant current of 30 mA cm^{-2} . The electrochemical uranium extraction performances were tested in an aqueous solution (50 mL) containing 100 mg L^{-1} of U(VI) and 30 g L^{-1} of F^- (F^- were sourced from KF electrolyte). The non-voltage adsorption experiments were tested on an unpowered three-electrode system in 50 mL of simulating nuclear water. The as-prepared $\text{Ti}(\text{OH})\text{PO}_4$ electrode, Pt wire, and Ag/AgCl electrode were also used as the working electrode, counter electrode, and reference electrode respectively. The condition of the adsorption test was similar to that of electrochemical extraction except for excluding external current or voltage. The effects of the initial concentration of uranium (from 50 to 600 mg L^{-1}), pH of the solution (from 4 to 10), interfering ions (including SO_4^{2-} , CO_3^{2-} , Cl^- , $\text{C}_2\text{O}_4^{2-}$, NO_3^- , NH_4^+), and the influence of F^- (from 5 to 30 g L^{-1}) on the electrochemical uranium extraction performance were measured in detail. The concentrations of the uranium and other cations in the electrolyte before and after electrolysis were determined by ICP-OES. The concentrations of the anions in the electrolyte before and after electrolysis were determined by IC. In the desorption process, the working electrode with extracted uranium was transferred into HCl aqueous solution (0.1 mol). The extraction experiments were conducted three times and the error bars were used in the curves. LSV and CV tests were performed in simulated nuclear wastewater at a scan rate of 10 mV s^{-1} .

Electrochemical uranium extraction experiments in real nuclear wastewater

The electrochemical uranium extraction experiments in real nuclear wastewater were measured with a typical two-electrode system. Graphite felt was cut into 5 cm \times 5 cm shapes as electrode substrates. $\text{Ti}(\text{OH})\text{PO}_4$ ion pair sites (40.0 mg), carbon black (8.0 mg), and Nafion Membrane solution (80 μL) were mixed with ethanol (8 mL) and sonicated for 1 h to form a homogeneous ink. The as-prepared ink was then uniformly brush-coated on graphite felt to prepare the working electrode, and Pt wire was used as the counter electrode. The uranium extraction was operated under a constant current of 30 mA cm^{-2} in 400 mL of real nuclear wastewater. The deposited electrode was immersed in ethanol and purified through an ultrasonic reaction, and

the powder was collected by drying. The proportions of metallic species in this powder were measured and analyzed by ICP-OES. The concentration changes of the uranium and other cations in real nuclear wastewater before and after electrolysis were determined by ICP-OES.

Uranium product purification

The purification of uranium was performed through a typical precipitation-calcination process. Initially, the uranium product from the electrochemical extraction was collected and dissolved in HCl. Subsequently, excess ammonia was added to the above solution to form a precipitate of ammonium diuranate. Finally, ammonium diuranate was collected by centrifugation and heated at 550 °C for 5 h to form a black-green uranium product.

Calculations

For quantifying the extraction efficiency (n , %), the uranium extraction capacity (q_e , mg g⁻¹), and adsorption energy (E_{ads} , eV) were calculated according to the following equations:

$$n = \frac{(C_0 - C_e)}{C_0} \quad (1)$$

Where C_0 (mg L⁻¹) and C_e (mg L⁻¹) represent the initial and final uranium concentration, respectively.

$$q_e = \frac{(C_0 - C_e) \times V}{m} \quad (2)$$

Where C_0 (mg L⁻¹) and C_e (mg L⁻¹) represent the initial and final uranium concentration, respectively; m (g) and V (L) denote the mass of the catalyst and volume of the electrolyte, respectively.

$$E_{\text{ads}} = E_{\text{AS}} - (E_{\text{S}} + E_{\text{A}}) \quad (3)$$

Where E_{AS} , E_{S} , and E_{A} are the total energies of the adsorbate-substrate (AS), substrate (S), and adsorbate (A), respectively.

Data availability

The data that supports the findings of the study are included in the main text and supplementary information files. Source data are provided with this paper. Source Data files are available in Figshare under accession code <https://doi.org/10.6084/m9.figshare.25603905>. Source data are provided with this paper.

References

- Chen, T. et al. Advanced photocatalysts for uranium extraction: elaborate design and future perspectives. *Coord. Chem. Rev.* **467**, 214615 (2022).
- Zhang, S., Li, H. & Wang, S. Construction of an ion pathway boosts uranium extraction from seawater. *Chem* **6**, 1504–1505 (2020).
- Tsouris, C. Uranium extraction: fuel from seawater. *Nat. Energy* **2**, 17022 (2017).
- Mei, D., Liu, L. & Yan, B. Adsorption of uranium (VI) by metal-organic frameworks and covalent-organic frameworks from water. *Coord. Chem. Rev.* **475**, 214917 (2023).
- Hu, Y. et al. Photochemically triggered self-extraction of uranium from aqueous solution under ambient conditions. *Appl. Catal. B: Environ.* **322**, 122092 (2023).
- Zhou, Y. et al. Amidoxime-functionalized MXene beads for the effective capture of uranium from wastewater with high fluoride concentrations. *Chem. Eng. J.* **471**, 144647 (2023).
- Ohashi, Y., Murashita, S. & Nomura, M. Extraction of uranium from solid waste containing uranium and fluorine. *Miner. Eng.* **61**, 32–39 (2014).
- Li, Z. et al. Exciton dissociation and transfer behavior and surface reaction mechanism in Donor-Acceptor organic semiconductor photocatalytic separation of uranium. *Appl. Catal. B: Environ.* **332**, 122751 (2023).
- Busquim e Silva, R., Kazimi, M. S. & Hejzlar, P. Nuclear fuel recycling: national and regional options for the US nuclear energy system. *Energy Environ. Sci.* **3**, 996–1010 (2010).
- Wang, C. et al. Uranium in situ electrolytic deposition with a reusable functional graphene-foam electrode. *Adv. Mater.* **33**, 2102633 (2021).
- Song, P. S., Min, B. Y., Choi, W. K., Jung, C. H. & Oh, W. Z. Effects of a slag former on the absorption of cerium and uranium oxide within a slag during a melting of stainless steel contaminated with uranium. *Sep. Purif. Technol.* **60**, 136–141 (2008).
- Xing, S., Luo, M., Wu, Y., Liu, D. & Dai, X. Rapid determination of uranium isotopes in calcium fluoride sludge by tandem quadrupole ICP-MS/MS. *J. Anal. Spectrom.* **34**, 2027–2034 (2019).
- Liu, C. et al. A half-wave rectified alternating current electrochemical method for uranium extraction from seawater. *Nat. Energy* **2**, 17007 (2017).
- Wang, Y. et al. Electrochemical-mediated regenerable Fe^{II} active sites for efficient uranium extraction at ultra-low cell voltage. *Angew. Chem. Int. Ed.* **62**, e202217601 (2023).
- Riedhammer, J., Halter, D. P. & Meyer, K. Nonaqueous electrochemistry of uranium complexes: A guide to structure-reactivity tuning. *Chem. Rev.* **123**, 7761–7781 (2023).
- Keener, M. et al. Redox-switchable carboranes for uranium capture and release. *Nature* **577**, 652–655 (2020).
- Liu, T. et al. Removal and recovery of uranium from groundwater using direct electrochemical reduction method: performance and implications. *Environ. Sci. Technol.* **53**, 14612–14619 (2019).
- Yang, H. et al. Functionalized iron-nitrogen-carbon electrocatalyst provides a reversible electron transfer platform for efficient uranium extraction from seawater. *Adv. Mater.* **33**, 2106621 (2021).
- Das, N., Das, A., Sarma, K. P. & Kumar, M. Provenance, prevalence and health perspective of co-occurrences of arsenic, fluoride and uranium in the aquifers of the Brahmaputra River floodplain. *Chemosphere* **194**, 755–772 (2018).
- Shen, J. & Schäfer, A. Removal of fluoride and uranium by nanofiltration and reverse osmosis: a review. *Chemosphere* **117**, 679–691 (2014).
- Miskowiec, A., Niedziela, J. L., Kirkegaard, M. C. & Shields, A. E. Analysis of water coupling in inelastic neutron spectra of uranyl fluoride. *Sci. Rep.* **9**, 10476 (2019).
- Li, X. et al. MXene chemistry, electrochemistry and energy storage applications. *Nat. Rev. Chem.* **6**, 389–404 (2022).
- Rosenkranz, A., Righi, M. C., Sumant, A. V., Anasori, B. & Mochalin, V. N. Perspectives of 2D MXene tribology. *Adv. Mater.* **35**, 2207757 (2023).
- Vahidmohammadi, A., Rosen, J. & Gogotsi, Y. The world of two-dimensional carbides and nitrides (MXenes). *Science* **372**, eabf1581 (2021).
- Robertson, D. D. & Tolbert, S. H. A direct and clean route to MXenes. *Science* **379**, 1189–1190 (2023).
- Zhang, X. et al. MXene aerogel scaffolds for high-rate lithium metal anodes. *Angew. Chem. Int. Ed.* **57**, 15028–15033 (2018).
- Sun, B. et al. Redox-active metaphosphate-like terminals enable high-capacity MXene anodes for ultrafast Na-ion storage. *Adv. Mater.* **34**, 2108682 (2022).
- Lei, J. et al. Enhanced photoreduction of U(VI) on WO₃ nanosheets by oxygen defect engineering. *Chem. Eng. J.* **416**, 129164 (2021).
- Zeng, Y. et al. Oxygen-vacancy and surface modulation of ultrathin nickel cobaltite nanosheets as a high-energy cathode for advanced Zn-ion batteries. *Adv. Mater.* **30**, 1802396 (2018).

30. Li, R. et al. Flexible and high-performance electrochromic devices enabled by self-assembled 2D TiO₂/MXene heterostructures. *Nat. Commun.* **12**, 1587 (2021).
31. Zhang, H. et al. MXene-derived Ti_nO_{2n-1} quantum dots distributed on porous carbon nanosheets for stable and long-life Li-S batteries: enhanced polysulfide mediation via defect engineering. *Adv. Mater.* **33**, 2008447 (2021).
32. Li, Y. et al. Synergetic effect of defects rich MoS₂ and Ti₃C₂ MXene as cocatalysts for enhanced photocatalytic H₂ production activity of TiO₂. *Chem. Eng. J.* **383**, 123178 (2020).
33. Al-Temimy, A. et al. Impact of cation intercalation on the electronic structure of Ti₃C₂T_x MXenes in sulfuric acid. *ACS Appl. Mater. Interfaces* **12**, 15087–15094 (2020).
34. Wang, P.-F. et al. Elucidation of the Jahn-Teller effect in a pair of sodium isomer. *Nano Energy* **77**, 105167 (2020).
35. Wang, Z. et al. Single-atom catalysts with ultrahigh catalase-like activity through electron filling and orbital energy regulation. *Adv. Funct. Mater.* **33**, 2209560 (2023).
36. Huang, J., Liu, Z., Huang, D., Jin, T. & Qian, Y. Efficient removal of uranium (VI) with a phytic acid-doped polypyrrole/carbon felt electrode using double potential step technique. *J. Hazard. Mater.* **433**, 128775 (2022).
37. Lv, S.-Y. et al. A non-polluting method for rapidly purifying uranium-containing wastewater and efficiently recovering uranium through electrochemical mineralization and oxidative roasting. *J. Hazard. Mater.* **416**, 125885 (2021).
38. Ye, Y. et al. Electrochemical removal and recovery of uranium: effects of operation conditions, mechanisms, and implications. *J. Hazard. Mater.* **432**, 128723 (2022).
39. Chen, T. et al. Ternary boron carbon nitrides hollow nanotubes with tunable p-n homojunction for photo-assisted uranium extraction: a combined batch, EXAFS and DFT calculations. *Appl. Catal. B: Environ.* **318**, 121815 (2022).
40. Chen, T. et al. Actinide-uranium single-atom catalysis for electrochemical nitrogen fixation. *Sci. Bull.* **67**, 2001–2012 (2022).
41. Kresse, G. & Furthmüller, J. Efficiency of ab-initio total energy calculations for metals and semiconductors using a plane-wave basis set. *Comput. Mater. Sci.* **6**, 15–50 (1996).
42. Kresse, G. & Furthmüller, J. Efficient iterative schemes for ab initio total-energy calculations using a plane-wave basis set. *Phys. Rev. B* **54**, 11169–11186 (1996).
43. Perdew, J. P., Burke, K. & Ernzerhof, M. Generalized gradient approximation made simple. *Phys. Rev. Lett.* **77**, 3865–3868 (1996).
44. Blöchl, P. E. Projector augmented-wave method. *Phys. Rev. B* **50**, 17953–17979 (1994).
45. Kresse, G. & Joubert, D. From ultrasoft pseudopotentials to the projector augmented-wave method. *Phys. Rev. B* **59**, 1758–1775 (1999).
46. Chadi, D. J. Special points for Brillouin-zone integrations. *Phys. Rev. B* **16**, 1746–1747 (1977).
47. Grimme, S., Antony, J., Ehrlich, S. & Krieg, H. A consistent and accurate ab initio parametrization of density functional dispersion correction (DFT-D) for the 94 elements H-Pu. *J. Chem. Phys.* **132**, 154104 (2010).

Acknowledgements

This work was supported by NSFC (No. U23A20105, R.H.; 22303002, Y.L.; 22106126, T.C.; and U2267224, W.Z.), the Open Fund of CNNC Key Laboratory for Uranium Extraction from Seawater (KLUES202201, W.Z.), the Project of State Key Laboratory of Environment-Friendly Energy Materials in SWUST (No. 20fksy19, W.Z.). Numerical computations were performed at Hefei Advanced Computing Center. The authors extend their gratitude to Shiyanjia Lab (www.shiyanjia.com) for providing invaluable assistance with the TEM and XPS analysis.

Author contributions

T.L. made the most important contributions, although all authors made contributions to the work. T.L., R.H., and W.Z. designed the studies and wrote the paper. T.L. and H.J. performed most of the experiments. T.C., H.Z., and K.H. provided advice and reagents. C.J. and Y.L. performed DFT calculations. R.H. and W.Z. supervised the research. All authors contributed to data analysis and commented on the manuscript.

Competing interests

The authors declare no competing interests.

Additional information

Supplementary information The online version contains supplementary material available at <https://doi.org/10.1038/s41467-024-48564-y>.

Correspondence and requests for materials should be addressed to Yan Liu, Wenkun Zhu or Rong He.

Peer review information *Nature Communications* thanks Changhyun Roh and the other, anonymous, reviewer for their contribution to the peer review of this work. A peer review file is available.

Reprints and permissions information is available at <http://www.nature.com/reprints>

Publisher's note Springer Nature remains neutral with regard to jurisdictional claims in published maps and institutional affiliations.

Open Access This article is licensed under a Creative Commons Attribution 4.0 International License, which permits use, sharing, adaptation, distribution and reproduction in any medium or format, as long as you give appropriate credit to the original author(s) and the source, provide a link to the Creative Commons licence, and indicate if changes were made. The images or other third party material in this article are included in the article's Creative Commons licence, unless indicated otherwise in a credit line to the material. If material is not included in the article's Creative Commons licence and your intended use is not permitted by statutory regulation or exceeds the permitted use, you will need to obtain permission directly from the copyright holder. To view a copy of this licence, visit <http://creativecommons.org/licenses/by/4.0/>.

© The Author(s) 2024